New Journal of Physics
The open access journal at the forefront of physics

Deutsche Physikalische Gesellschaft DPG
IOP Institute of Physics

Published in partnership with: Deutsche Physikalische Gesellschaft and the Institute of Physics

OPEN ACCESS

RECEIVED
1 November 2018

REVISED
19 February 2019

ACCEPTED FOR PUBLICATION
15 March 2019

PUBLISHED
24 April 2019

Original content from this work may be used under the terms of the Creative Commons Attribution 3.0 licence.

Any further distribution of this work must maintain attribution to the author(s) and the title of the work, journal citation and DOI.

PAPER

Interaction of relativistically intense laser pulses with long-scale near critical plasmas for optimization of laser based sources of MeV electrons and gamma-rays

O N Rosmej[1,2], N E Andreev[3,4], S Zaehter[2], N Zahn[2], P Christ[2], B Borm[1,2], T Radon[1], A Sokolov[1], L P Pugachev[3,4], D Khaghani[5], F Horst[1,6], N G Borisenko[7], G Sklizkov[7] and V G Pimenov[8]

[1] Helmholtzzentrum GSI-Darmstadt, Planckstr.1, D-64291 Darmstadt, Germany
[2] Goethe University, Frankfurt, Max-von-Laue-Str. 1, D-60438 Frankfurt am Main, Germany
[3] Joint Institute for High Temperatures, RAS, Izhorskaya st.13, Bldg. 2, 125412 Moscow, Russia
[4] Moscow Institute of Physics and Technology (State University), Institutskiy Pereulok 9, 141700 Dolgoprudny, Moscow Region, Russia
[5] Institute of Optics and Quantum Electronics, Abbe Center of Photonics, Friedrich Schiller University Jena, Max-Wien-Platz 1, D-07745 Jena, Germany
[6] THM University of Applied Sciences, Wiesen Str. 14, D-35390 Giessen, Germany
[7] P N Lebedev Physical Institute, RAS, Leninsky Prospekt 53, 119991 Moscow, Russia
[8] N D Zelinskiy Institute of Organic Chemistry, RAS, Leninsky Prospekt 47, 119991 Moscow, Russia

E-mail: o.rosmej@gsi.de

Keywords: relativistically intense laser pulses, NCD-plasmas, low density polymer aerogels, super-sonic ionization, super-ponderomotive electrons, gamma-rays

Abstract

Experiments were performed to study electron acceleration by intense sub-picosecond laser pulses propagating in sub-mm long plasmas of near critical electron density (NCD). Low density foam layers of 300–500 μm thickness were used as targets. In foams, the NCD-plasma was produced by a mechanism of super-sonic ionization when a well-defined separate ns-pulse was sent onto the foam-target forerunning the relativistic main pulse. The application of sub-mm thick low density foam layers provided a substantial increase of the electron acceleration path in a NCD-plasma compared to the case of freely expanding plasmas created in the interaction of the ns-laser pulse with solid foils. The performed experiments on the electron heating by a 100 J, 750 fs short laser pulse of $2–5 \times 10^{19}$ W cm^{-2} intensity demonstrated that the effective temperature of supra-thermal electrons increased from 1.5–2 MeV in the case of the relativistic laser interaction with a metallic foil at high laser contrast up to 13 MeV for the laser shots onto the pre-ionized foam. The observed tendency towards a strong increase of the mean electron energy and the number of ultra-relativistic laser-accelerated electrons is reinforced by the results of gamma-yield measurements that showed a 1000-fold increase of the measured doses. The experiment was supported by 3D-PIC and FLUKA simulations, which considered the laser parameters and the geometry of the experimental set-up. Both, measurements and simulations showed a high directionality of the acceleration process, since the strongest increase in the electron energy, charge and corresponding gamma-yield was observed close to the direction of the laser pulse propagation. The charge of super-ponderomotive electrons with energy above 30 MeV reached a very high value of 78 nC.

1. Introduction

The experimental investigation of high energy density (HED) matter states created with intense laser [1, 2] and heavy ion beams [3, 4] requires active backlighting with highly penetrating gamma-rays and energetic particles that provide important diagnostic tools to access plasma parameters and structural information from inside the high areal density samples. Intense and well directed beams of photons with energies far above 100 keV and energetic particle beams of electrons/protons of tens to hundreds of MeV are the best candidates for such

© 2019 The Author(s). Published by IOP Publishing Ltd on behalf of the Institute of Physics and Deutsche Physikalische Gesellschaft

radiographic applications. TW and PW-class lasers systems that deliver laser pulses of relativistic intensities are widely used to generate relativistic particle beams and gamma-radiation. A micrometer-small size laser focus on a target surface and a short laser pulse duration ensure high radiographic potential of these secondary sources. By providing up to 10 micrometer spatial resolution and snap shots of the WDM-object density distribution in ps- up to fs-time scale, the analysis of the hydrodynamic motion of heated matter is facilitated [5, 6].

Electrons play a major role at the very first stage of laser-matter interaction that lead to production of laser based sources of radiation and particles. There are different mechanisms of laser energy transfer to high energy electrons depending on the laser parameters and the type of targets. The targets range from solid density with sharp boundaries to extended low density gas. In solids, the mechanism strongly depends on the gradients of the pre-plasma on the target surface and can be the vacuum/Brunel [7], resonant absorption in critical density, the ponderomotive and the ($J \times B$) mechanism of acceleration [8, 9] or stochastic heating [10–13] etc. Laser interaction with low density gas targets provides an effective acceleration of electrons to high energies in the wakefields generated in preformed plasma channels [14–16]. Great results have been achieved in the generation of monoenergetic electron beams. For instance, in experiments on the interaction of relativistic laser pulses with low density gas jets and capillary plasmas, the obtained energies range from hundreds of MeV up to several GeV [17–20]. Nevertheless, the charge carried by these electron beams does not exceed tens of pC, which is not sufficient to radiograph HED-samples in experiments with a high level of background radiation.

One of the possibilities to increase the electron beam charge above a nC level keeping the electron energy at a level of tens up to hundreds of MeV, is to use the advantage of relativistic laser interaction with plasmas of subcritical and near critical density (NCD) [21–24]. The critical electron density is defined as $n_{cr} = m\omega_L^2/(4\pi e^2)$ where m and e are the mass of electron at rest and its charge and ω_L is the laser frequency.

One of the first theoretical works that discusses particle acceleration in relativistic laser channels generated in near critical plasmas is based on results of 3D PIC-simulations [25]. Simulations demonstrated effects of channeling and filamentation of the relativistic laser pulse in the NCD-part of expanding plasma and generation of a strong current of energetic, 10–100 MeV electrons that have Boltzmann-like energy distribution with an effective temperature, which depends among others on the laser pulse intensity and the length of the NCD plasma region. This strong electron current is accompanied by the creation of a giant azimuthal quasi-static magnetic field [25, 26]. The mechanism of the electron acceleration in NCD plasmas has intrinsically complex nature, as it involves many physical processes simultaneously. In [25], the authors propose a mechanism of the direct laser energy coupling into hot electrons that occurs in relativistic laser channels. This coupling requires strong self-generated static electric and magnetic fields that confine fast electrons in relativistic channels. The electrons experience transverse betatron oscillations that provide an efficient energy exchange when the betatron frequency becomes close to the Doppler shifted laser frequency [25]. The effective electron temperatures obtained numerically for the case of the relativistic laser interaction with expanding plasmas, described by the exponential electron density profile with the scale length $L = 30$ μm was 4.5 MeV for $I_L = 10^{19}$ W cm^{-2} and 14 MeV for $I_L = 10^{20}$ W cm^{-2}.

After Pukhov [25], extended analysis of the relativistic laser pulse interaction with sub-critical plasmas was made by Arefiev and Khudik *et al* [27, 28]. They examine the processes of direct laser acceleration (DLA) of relativistic electrons undergoing betatron oscillations in a plasma channel and the role played by transverse and longitudinal quasi-static electric fields. In [28], a universal scaling for the maximum attainable electron energy was derived analytically. Moreover, the authors have shown a threshold dependence of the final energy gain on the laser intensity.

Up to now, only few experiments have been performed to demonstrate the advantages of the discussed mechanism of the electron acceleration. The energy transfer from an ultra-intense laser pulse with an intensity of 10^{20} W cm^{-2} to hot electrons in NCD plasmas depending on the pre-plasma scale length [29] was partially investigated experimentally and partially using 2D PIC-simulations. In order to produce an one-dimensional expansion of the plasma with a well-controlled scale length, a separate 5 ns long laser pulse with a 100 μm large focal spot was used. In the experiment, the coupling of the energy of the ultra-intense laser pulse into hot electrons was analyzed indirectly using measurements of Cu Kα-intensity and proton spectra depending on the pre-plasma scale length that in turn was simulated in 1D approximation for different energies of the long pulse. The energy distribution of energetic electrons was not measured directly but simulated using a 2D PIC-code. A discovered one order of magnitude variation in the coupling efficiency of the laser energy into fast electrons was explained by the existence of a density gradient optimum that ensures strong laser pulse self-focusing and channeling processes.

Measurements of electrons accelerated by a relativistic laser pulse propagating across a mm-long extended sub-NCD plasma plume were reported in [22]. The experiments showed a strong increase of the 'temperature' and number of supra-ponderomotive electrons caused by the increased length of a relativistic ion channel. New results on the electron acceleration from pre-ionized foam layers conducted at the Titan laser system were reported in [24]. There, 250 μm thick foam layers with mean densities from 3 up to 100 mg cm^{-3}

($n_e = 0.9$–30×10^{21} cm^{-3}) were pre-ionized by ns ASE-prepulse. The 1 kJ, 8–10 ps short laser pulse had $(5.3 \pm 1.8) \times 10^{19}$ W cm^{-2} intensity. An approximation of the high energy tail of the measured electron spectra with a Maxwell-like function resulted in 2 up to 4 times higher effective electron temperatures than $U_{\rm pond} \backsimeq 5.4$ MeV for $a_L = 6.5$.

The production of a hydrodynamically stable NCD-plasma layer remains an important issue for such type of experiments. 3D PIC simulations of the relativistic laser interaction with large-scale NCD plasmas [30, 31] demonstrated that low density CHO aerogel [32–34] is a very prospective material for creation of sub-mm long NCD plasmas and efficient electron acceleration. In the preparation of the reported here experimental campaign, an optimization study was performed for the range of current PHELIX-laser parameters and various areal densities of the NCD-plasmas [30]. Results of 3D-PIC-simulations demonstrated effects of self-focusing and filamentation of the laser pulse, the formation of relativistic plasma channels, their bifurcation and the generation of strong quasi-static magnetic field. It was shown that part of the energy spectrum of accelerated electrons can be approximated by the ponderomotive scaling with laser pulse amplitude increased up to three times due to the self-focusing effect in the NCD-plasma. Additional acceleration of electrons to higher energies was explained by the energy gain directly from the high-frequency laser field (DLA) in the emerging plasma channel where a quasi-static azimuthal magnetic field can keep electrons during the acceleration process.

In this article, we present new experimental results on the interaction of relativistic sub-picosecond laser pulses with sub-mm long NCD plasmas. Polymer foam layers of 2 mg cm^{-3} density and up to 500 μm thickness were used to create hydrodynamically stable, large scale, quasi-homogeneous plasmas targets. The NCD-plasma was produced by a mechanism of a super-sonic ionization when a well-defined ns-pulse with 1–3 J energy was sent onto the foam target forerunning the relativistic main pulse. The energy and the duration of the ns-pulse were well matched to the mean volume density and the thickness of foam layers in order to optimize the velocity of the supersonic ionization wave that creates high aspect ratio NCD plasma. Note that even higher hydrodynamic (HD) stability of the plasma slab can be reached if CHO-foam layer is heated not directly by ns-laser pulse, but by x-rays generated due to interaction of ns laser pulse with an Au-hohlraum [35–37]. In this case, the electron temperature in the plasma reaches moderate 20–40 eV and a mean ion charge $Z = 2.3$ (instead of 4.3 in the case of fully ionized CHO-atoms). Great advantage of this indirect laser heating is a very stable HD-behavior of the plasma layer up to 10 ns after the laser energy deposition into the Au-hohlraum. This method can be applied if the energy of the ns pulse is large enough to generate a hohlraum radiation temperature above 30–40 eV. If the energy of the ns-pulse is restricted or one uses ns-prepulse to drive a super-sonic ionization, like it was done in [24], direct laser irradiation of the foam layers has to be used.

Direct measurements of the electron energy distribution were performed by means of two electron spectrometers with a static magnetic field. By comparing shots onto metallic foils and onto pre-ionized low density foam layers, it was demonstrated that the effective temperature of supra-thermal electrons increased from 1.5 to 2.2 MeV, in the case of the relativistic laser interaction with a metallic foil at high laser contrast, up to 13 MeV for the laser shots onto the pre-ionized 300 and 500 μm thick foam layers. A strong increase of the mean electron energy and number of ultra-relativistic electrons was reinforced by the results of the gamma-yield measurements. In the case of pre-ionized polymer foams, a 1000-fold increase of the measured doses in all 10 channels of the gamma-spectrometer covering the photon energy range from 30 keV up to 100 MeV was shown. For interpretation of the measured doses by means of the Monte Carlo multi-particle transport code FLUKA, the electron spectra were approximated by a Maxwell-like distribution with two effective temperatures. The best fit of the measured values obtained with a deviation less than 10% resulted in $T_1 \backsimeq 12$ MeV and $T_2 \backsimeq 2$–5 MeV, which is in a good agreement with direct measurements made by means of two electron spectrometers.

The experiment was supported by 3D-PIC simulations that considered the used laser parameters and the geometry of the experimental set-up. Moreover, it was thereby possible to simulate the absolute number of accelerated electrons, their energy and angular distributions, which was in a good agreement with measurements. The simulations and the measurements showed a high directionality of the acceleration process, since the strongest increase of the electron energy, charge and corresponding gamma-yield was observed close to the direction of the laser pulse propagation.

The paper is organized as follows: laser and target parameters together with the used experimental set-up are described in section 2; angle dependent measurements of the electron spectral distribution and dosimetry of hard bremsstrahlung radiation are presented in sections 3; and in 4, PIC-simulations taking into account for the experimental geometry are compared with the experiment; section 5 summarizes the experimental results and results of the modeling.

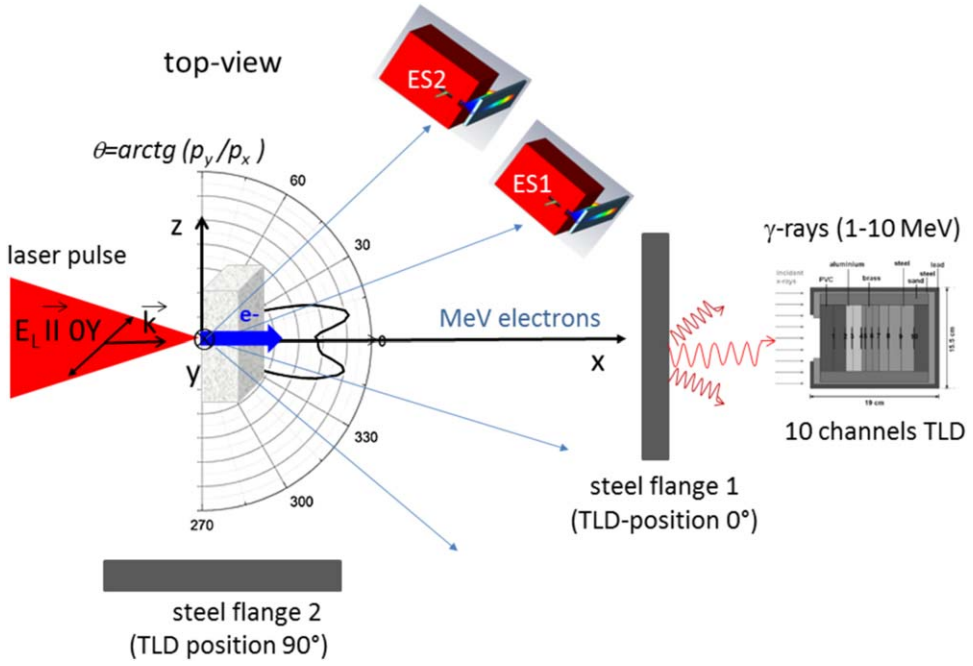

Figure 1. Experimental scheme: orientation of the laser beam relative the target; electron spectrometers ES1 and ES2 placed in the horizontal plane under 18° and 44° to the laser pulse propagation direction along the *x*-axis; and a ten channel TLD-detector for characterization of the gamma-radiation spectral distribution.

2. Experimental set-up

The goal of the performed experiments was to study the electron acceleration by intense sub-picosecond laser pulses propagating in sub-mm long plasmas of near critical electron density (NCD) and characterization of the energy distribution of super-ponderomotive electrons. In [30, 31], it was shown that the interaction of relativistic laser pulses with foam targets of NCD provides an efficient conversion of the laser energy into relativistic electron beams with energies far above those predicted by Wilks [9] $T_h = mc^2(\sqrt{a_L^2 + 1} - 1)$ where a_L is the normalized vector potential, $a_L^2 = 0.73 I_{L,18}\lambda_\mu^2$, $mc^2 = 511$ keV, $I_{L,18}$ is the laser peak intensity in units of 10^{18} W cm^{-2}, and λ_μ is the laser wave length in μm. Distinctive features of these beams are their up to 100 MeV high energy accompanied by a large number of electrons (tens of nC) and a strong directionality. This prediction was realized experimentally by the application of under-dense polymer foams while keeping the laser parameters fixed. Our experiments were performed at the Nd:glass PHELIX-laser facility at the Helmholtzzentrum GSI-Darmstadt, Germany. A *s*-polarized laser pulse of 1.053 μm fundamental wavelength, 80–100 J energy and 750 $\pm$ 250 fs pulse duration was focused onto the target by means of a 150 cm 90° off-axis parabola under 5° to the target normal. In this way, up to 60% of the laser energy was concentrated in the focal spot with a FWHM-size of $14 \pm 1 \times 19 \pm 1$ μm^2. Shot-to-shot deviations of the laser energy and 30% uncertainties in the laser pulse duration resulted in the rather large confidential interval of the laser intensities ranging from 2.1 up to 5.1×10^{19} W cm^{-2}. The corresponding normalized vector potentials are $a_L = 3.9$–6.0. The ns laser contrast was kept at the highest level between 10^{-11} and 10^{-12}.

As targets low density polymer aerogels (foams) with 2 mg cm^{-3} volume density and conventional metallic foils (Cu, Ti) were used. In order to create the NCD plasma, a foam layer/foil was irradiated by a 1.5 ns long pulse with a triangular temporal shape and 1–3 J energy forerunning the relativistic short main pulse. The delay between the peak of the ns pulse and the relativistic main pulse was varied from 0 up to 5 ns.

The top-view of the experiment is presented in figure 1. The diagnostics set-up included two portable electron spectrometers with 250 mT static magnets. The spectrometers were placed in the target chamber in a horizontal plane perpendicular to the laser polarization vector. The distance between the interaction point and the entrance holes of both spectrometers was 450 mm. In order to measure an angular distribution of super ponderomotive electrons predicted in simulations [30], the first spectrometer ES1 was placed under 18° and the second one (ES2) under 44° to the laser pulse propagation direction (*x*-axis, figure 1).

A thermo-luminescence dosimetry (TLD)-based ten channel system was used for the spectrometry of the hard bremsstrahlung caused by MeV electrons interacting with a 17 mm thick Fe-flange that separated the evacuated target chamber from the environment. Ten TLD-cards were placed inside a shielding cylinder with a collimator window between the absorbers, which are manufactured from lower to higher *Z* materials of different

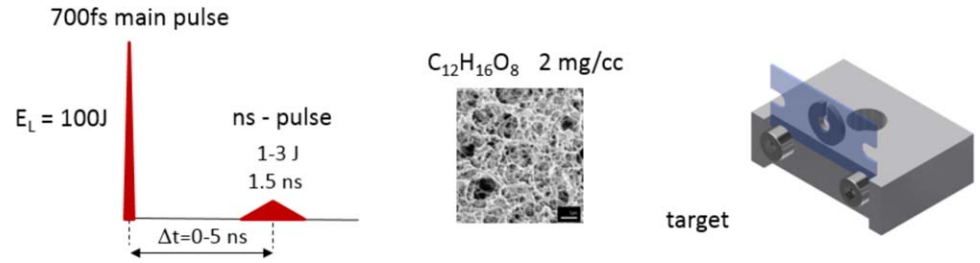

Figure 2. Combination of a low energy ns-pulse and a sub-ps main-pulse (left), high resolution image of the TAC-structure (center) and a target station used in the experiment (right).

thickness [38]. The incident x-rays penetrate different absorbers and cause a corresponding TLD-signal (dose) in all ten cannels. The spectrometer was designed for an energy range from 30 keV up to 100 MeV. The TLD-detector was placed for one set of shots in the direction of the laser pulse propagation and for another set in perpendicular direction to measure an angular dependence of the MeV bremsstrahlung radiation produced by supra-thermal electrons.

In order to produce high aspect ratio homogeneous plasma with a slightly under-critical electron density, 2 mg cm^{-3} cellulose triacetate (TAC, $C_{12}H_{16}O_8$) layers with thicknesses of 300 and 500 μm were used [32–34]. TAC-layers are optically transparent and characterized by a highly uniform 3D network structure consisting of 1–2 μm pores, 0.1 μm thick and 1 μm long fibers with density of approximately 0.1 g cm^{-3}. The density fluctuations on the focal-spot size area of 100 $\times$ 100 μm^2 do not exceed 0.5%. Due to their open cell structure, air contained by pores can be evacuated. The mean volume density of 2 mg cm^{-3} TAC-foam corresponds to 1.7×10^{20} atoms cm^{-3} and a mean ion charge $Z_{\mathrm{mean}} = 4.2$. Full ionization of all CHO-atoms would correspond to an electron density of 7×10^{20} cm^{-3}, which is slightly lower than critical density (10^{21} cm^{-3}) for the fundamental wavelength of the Nd:glass laser ($\lambda = 1.053$ μm).

When the laser interacts with the foam surface, it starts to heat and the solid membranes/fibers get ionized. The plasma created by the ionization of 0.1 g cm^{-3} (8×10^{21} atoms cm^{-3}) dense, 100 nm thick fibers has an overcritical electron density and the fiber thickness is larger than the thickness of the skin layer (~30 nm). Consequently, it takes time until the created plasma will expand into the pores reaching undercritical electron density and allowing further propagation of the laser pulse into the 3D-like aerogel structure. The intensity of the ns-pulse can be matched to the target density and target thickness in such a way that the velocity of the ionization front will be much faster than the ion acoustic velocity. During the propagation of the supersonic ionization wave, the heated high aspect ratio plasma region does not undergo notable expansion.

It was shown analytically [39] and experimentally [40] that the velocity of the super-sonic ionization front propagation in an initially porous matter is lower than in a homogeneous medium of sub-critical density, like in a gas. Estimations of the ionization front propagation velocity V_p that considered the delay caused by hydro-homogenization processes on the micrometer scale have been made in accordance with equation (27) in [37]

$$V_p \approx 9.7 \times 10^4 \frac{A^{\frac{2}{3}} I_{14}^{\frac{1}{3}}}{Z_m^{\frac{2}{3}} \lambda_L^{\frac{4}{3}} \rho_a^{\alpha} \rho_s^{1-\alpha}}, \ \mathrm{cm\ s^{-1}}$$

for the following values that describe the laser parameters and $C_{12}H_{16}O_8$ foam structure used in the experiment: mean $A = 8$; mean ion charge $Z_m = 4.2$, mean foam density $\rho_a = 2$ mg cm^{-3}, fiber density $\rho_s = 0.1$ g cm^{-3}, laser wave length $\lambda_L = 1$ μm, normalized to 10^{14} W cm^{-2} laser intensity $I_{14} = 0.5$ and a power factor $\alpha = 0.8$ that reflects the geometry of the foam structure [39]. The velocity of the ionization front amounts $V_p = 2 \times 10^7$ cm s^{-1} and an estimated time required for ionization of a 300–500 μm thick foam layer by the 1 J ns-pulse reaches 1.5–2.5 ns. Due to the fact that the foam-targets were enclosed into Cu-washers (see target station in figure 2) we could not measure experimentally the electron density profile to the time of relativistic pulse arrival. We can assume that at a large delay between the ns- and main pulses, the front part of the created plasma expands toward the incident laser. PIC-simulations made for a plasma layer with a constant NCD electron density and for a combination of the linear density profile with a density plateau showed no noticeable difference in the electron energy distribution and charge.

In the case of metallic foils, an inhomogeneous plasma plume that expands toward the main laser pulse with an exponentially decaying electron density was produced by the same 1–3 J ns pulse forerunning the relativistic short main pulse with the delay varied from 0 up to 5 ns.

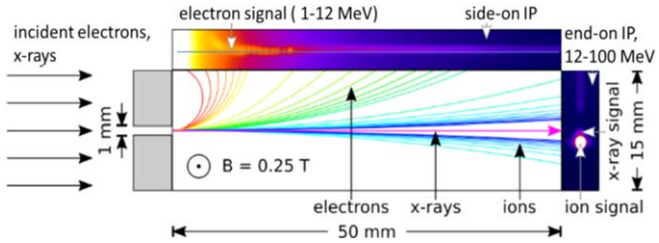

Figure 3. Scheme of the electron spectrometer.

3. Experimental results

The laser shots that we analyze here were made onto Cu-foils and CHO-foams at 10^{-11} ns laser contrast with and without an additional nanosecond pulse. The results of electron spectra measured by two electron spectrometers ES1 and ES2 and the TLD-dose caused by the bremsstrahlung radiation were very stable from shot to shot for every type of laser pulse and target combination.

3.1. Electron spectra

For the measurements of the electron energy distribution, two electron spectrometers with a 250 mT nominal static magnetic field were used. The principal scheme of the electron spectrometer is shown in figure 3. The spectrometer consisted of an iron housing that held two imaging plates (IPs). A signal on the long, side-on IP corresponds to electron energies $1 < E < 12$ MeV and the short, end-on IP covers the electron energy range from 12 MeV up to 100 MeV. A 2D-map of the magnetic field distribution inside the spectrometer at the height of the entrance hole was made by means of a hall-probe. In the center of the Neodym-magnets the measured B-field reached 245–250 mT with a gradient of 2–5 mT mm^{-1}. The B-field dropped down to 190 mT at a distance of 1 mm from the magnet edges. The dispersion curve that accounts for this gradient dynamics was used to simulate electron trajectories. The response of BASF MS IPs to an electron impact accounting for the electron energy and angle of incidence was taken from [41, 42].

Raw electron spectra for high contrast shots onto Cu-foil (sh.30), shot onto the Cu-foil with a well-defined ns-pulse (sh. 27), and onto 300 and 500 μm thick CHO-foam targets (sh. 31, 34, 38, 44) pre-ionized by the ns-pulse are presented in figure 4. The signals measured by the electron spectrometer ES1 placed 18° to the laser pulse propagation direction are shown on the left side of figure 4 and those measured by ES2 under 44° on the right side of figure 4. Two spots in the middle of the end-on IP (see e.g. figure 4, sh.31, ES1) are produced by x-rays (low intensity signal) and MeV-protons (saturated signal) that experience only a slight deviation in the magnetic field. The position of the x-ray signal would correspond to infinitely large electron energy.

In figure 4, one observes a low background signal on the long, side-on IP (electron energies $E \lesssim 12$ MeV) for shots onto foils at a high laser contrast (sh. 30) and an increased amplitude of the IP signal and higher electron energies in the case of a shot onto pre-ionized Cu-foil (sh.27). In the case of sh.27, a three times smaller entrance hole (0.3 mm instead of 1 mm) was mounted onto ES1-spectrometer, so that the amplitudes of ES1 and ES2 signals are not comparable. Nevertheless, one can clearly observe the appearance of high energy tails in both signals.

The saturated IP signal in the case of the laser irradiation of foams (sh. 31, 34, 38, 44), which was regularly detected in the IP-region with electron energies below 1 MeV, is probably caused by a strongly increased amount of laser accelerated electrons with $E > 6$–8 MeV. These electrons having a large stopping range, penetrated directly the 5 mm thick front iron-wall of the electron spectrometer and were deflected by magnetic field in accordance with their final energy. We excluded this energy region from our analysis and present results for electrons that entered the spectrometer through the 1 mm collimator hole with energies above 4 MeV.

A rather poor dispersion of the end-on IP, where signals from electrons with energies between 12 and 100 MeV are accumulated, still allowed for the registration of the pronounced effect of the effective laser energy coupling into electrons in NCD-plasmas and their acceleration up to tens of MeVs (see raw electron spectra measured by ES1 end-on IP for shots 31, 34, 38, 44). Data from the absolute calibration of the image plates for relativistic electrons with energies up to 10 MeV and the dependence of the absolute signal on the electron angle of incidence onto the IP [41, 42] were used to evaluate the number of electrons in different energy ranges. Additionally, the IP-signal was corrected for energies above 10 MeV where the stopping power increases by a factor of 2 between 10 and 100 MeV due to radiation losses. Experimental energy distributions of electrons with energies between 4 and 80 MeV that entered the spectrometer through the 1 mm collimator hole are presented

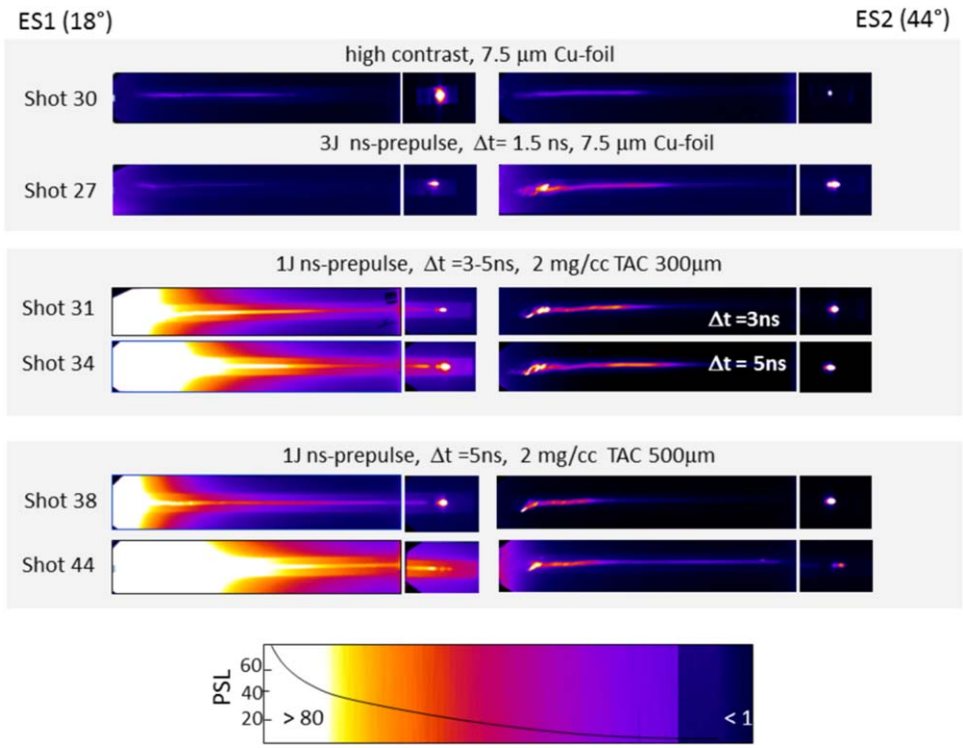

Figure 4. Raw electron spectra measured by means of electron spectrometers ES1 and ES2 under 18° and 44° to the laser propagation direction for various combinations of the ns-pulse energy and the delay Δt between the ns- and short pulses. The color scale of the IP signal expressed in photo-stimulated luminescence (PSL) is the same for all presented spectra.

in figure 5(a). Figure 5(b) shows the total number of electrons that entered the spectrometer with energies above the given one.

The measured electron spectra were fitted by several Maxwell-like distributions with different temperatures (dashed lines in figure 5(a)). One part of the electron spectra that can be well approximated by a ponderomotive 'temperature' of 1.5–3 MeV is present in all shots onto the foil and CHO-foams under 18° and 44°. When shooting onto the pre-ionized foams, we observe at least a 10-fold increase of the number of hot electrons with $E < 10$ MeV measured by ES1 and ES2 and a dramatic increase of the number of ultra-relativistic electrons with energies above 20 MeV (sh. 34, 44, figure 4) measured by means of ES1 under 18°.

The maximum of the effective electron temperature $T_h \backsimeq 13$ MeV was achieved in the case of 300 μm and 500 μm thick pre-ionized CHO-foam layers of 2 mg cm^{-3} mean density and 5 ns delay between the pre-pulse and the main pulse (e.g. sh. 34, 44). This is at least 5–8.6 times higher than predicted by Wilks scaling determined by the vacuum laser pulse intensity 2.1–5.1 $\times$ 10^{19} W cm^{-2} ($T_h = 1.55$–2.60 MeV) and measured in the high contrast laser interaction with Cu-foils ($T_h = 1.57$–2.23 MeV, e.g. sh. 30). The energy distribution of electrons detected under 18° and 44° is very similar in the case of shots with a high laser contrast (compare raw spectra and electron energy distribution measured by ES1 and ES2 in sh.30, figure 4). By interaction of the relativistic laser pulse with low density foams pre-ionized by the ns-pulse, we observe a predominant effect in the electron spectra measured by ES1 (figures 4, 5) under 18° to the laser propagation direction. An approximation of the high energy tails ($E >$ 25–30 MeV) with a Maxwell-like distribution function results into 12.8–13 MeV effective electron temperature, while the measured number of electrons with energies $E > 30$ MeV that entered the spectrometers trough the 1 mm hole reached 3 $\times$ 10^5 particles (figure 5(b)). The IP signal of the electron spectra measured by ES2 caused by electrons with $E >$ 25–30 MeV is at the background level (figures 5(a), (b)).

3.2. Measurements of the TLD-doses caused by bremsstrahlung radiation

The observed tendency towards the strong increase of the mean electron energy and number of MeV laser-accelerated electrons is reinforced by the results of the gamma-yield measurements.

The bremsstrahlung radiation (BS) was produced by MeV electrons passing through a 17 mm thick steel flange, located at a distance of 868 mm from the target in the laser pulse direction. An absolute calibrated ten-channel TLD-spectrometer [38] based on the method of thermo-luminescence dosimetry was used as a measurement tool for the bremsstrahlung. The ten TLD-cards were placed between absorbers inside a shielding cylinder with a collimator window. These absorbers having different thicknesses were fabricated from different

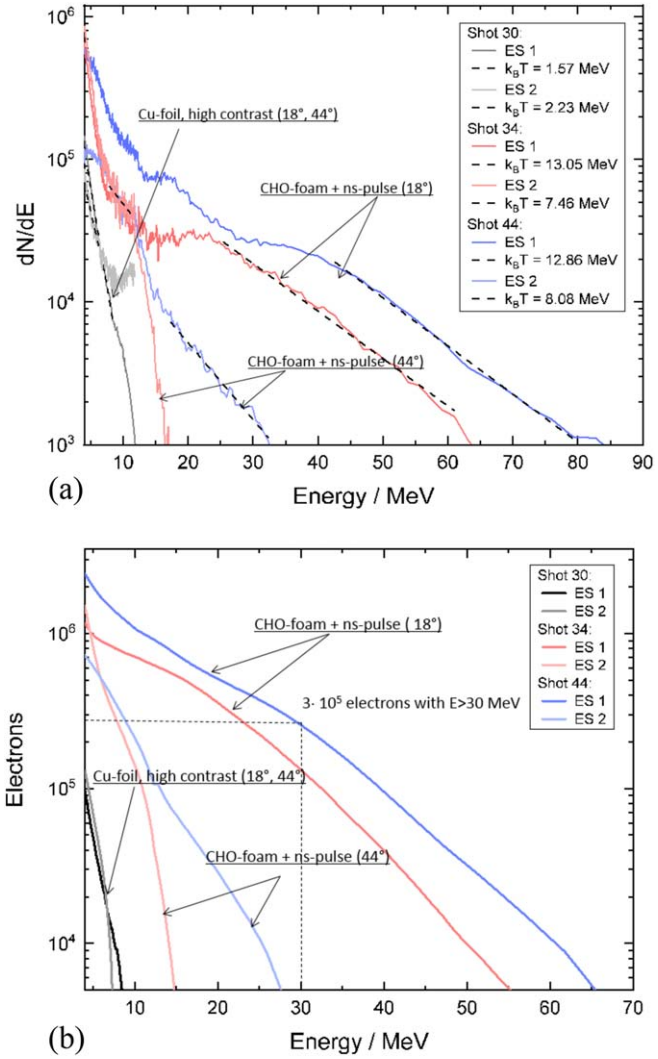

Figure 5. (a) Energy distribution of electrons with energies from 4 up to 80 MeV that entered the spectrometer; (b) evaluated total number of electrons that enter the spectrometer with energies above the given one.

materials of increasing Z ranging from PVC to steel. The materials of the TLD cards are pieces of doped lithium fluoride in two variations: TLD 700 (7LiF: Mg, Ti) and TLD 700 H (7LiF: Mg, Cu, P). They are suitable for the detection of fast pulsed radiation. The response of the detectors is based on the excitation of the decoupled atoms. TLDs absorb radiation and emit photons proportionally to the deposited dose when heated to a few hundred degrees Celsius and have reduced residual signal. TLD 700 H cards were calibrated for low- to high-dose ranges from 1 μGy to 20 Gy and have a very good dose-response and linearity at much higher doses. The spectrometer is designed for an energy range from 30 keV to 100 MeV, resolved in 10 different energy bins. The widths of the ten energy bins with $j = 1$–10 are: $\Delta E_j = [0.02; 0.05; 0.15; 0.25; 0.5; 1.5; 2.5; 5.0; 40; 50]$ MeV with corresponding interval centers: $E_j = [0.04; 0.075; 0.175; 0.375; 0.750; 1.75; 3.75; 7.5; 30.0; 75.0]$ MeV.

Figures 6(a) and (b) show the measured dose readings that were obtained by the 10-channel TLD-spectrometer for laser shots generated at different conditions; target type, high contrast interaction or application of the ns-pulse prior to the relativistic main pulse and position of the TLD-spectrometer: (a) at 0° and (b) at 90° to the laser pulse propagation direction.

When the TLD-spectrometer was placed at 0°, the lowest dose values were measured for shots onto Cu-foils (sh. 4, 25, 28) and 500 μm thick CHO-foams (sh. 37) that used the high ns contrast $\lesssim 10^{-11}$, see figure 6(a). For high contrast laser shots no dependence of the TLD-doses on the target material and the target structure was measured. Shots 1, 2 deal with the case when the main laser pulse interacts with expanded plasma created by the ns-pulse that hit the Cu-foil.

The density profile of the expanded plasma comprises a relatively short NCD-region, in which effective electron acceleration takes place. Experimentally, we observe a strongly increased level of EMPs in the laser-bay outside the target chamber and one order of magnitude increase in the dose of the gamma-radiation measured by the TLD-detectors.

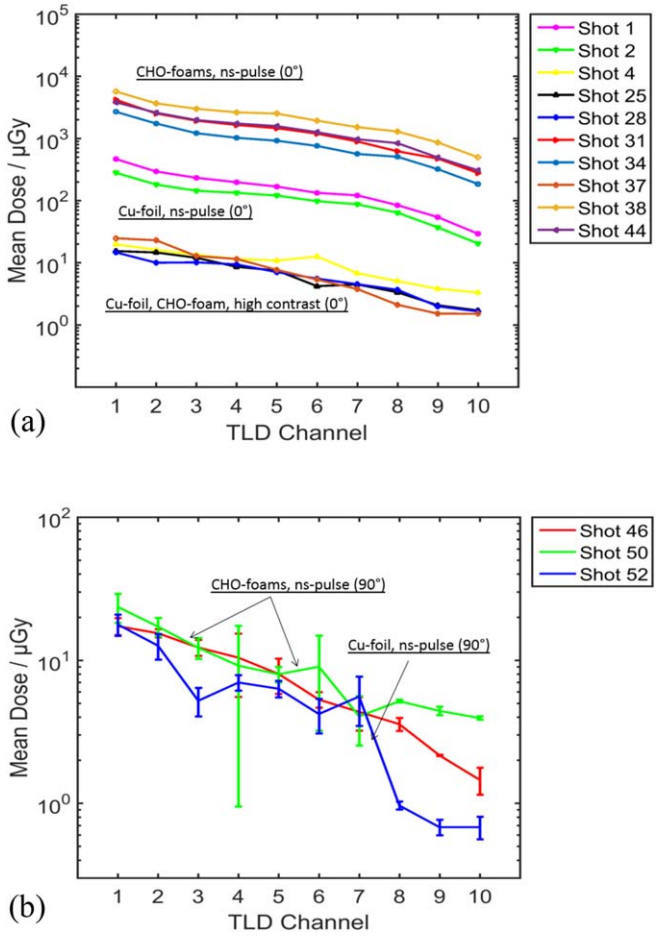

Figure 6. (a) Doses registered by the ten-channel TLD-spectrometer placed in the direction of the laser pulse propagation for shots made at different conditions; (b) same measurements made in the direction perpendicular to the laser pulse propagation.

At relativistic laser interaction with pre-ionized CHO-foams, the creation of the 300–500 μm long NCD plasmas ensures a longer acceleration path than in the case of freely expanding plasmas, which results in an even more effective coupling of the laser energy into energetic electrons. For example, this effect was clearly observed in the shots 31, 34, 37, 38, 44, where the relativistic laser pulse interacted with pre-ionized CHO-foam. TLD-measurements made in the direction of the laser pulse after its propagation through the long scale NCD-plasma showed a 1000-fold increase of the measured doses in all 10 channels compared to the high contrast case.

In the perpendicular direction (figure 6(b)), the measured TLD doses in the case of pre-ionized Cu-foil (sh. 52) and CHO-foam layers (sh. 46, 50) are very similar. The dose values are close to those measured in the direction of the laser pulse propagation at high laser contrast (figure 6(a)).

The dose readings measured in the different channels of the TLD-spectrometer resulted from contributions made by photons and electrons with different energies. Consequently, the deconvolution of the spectral distributions of the electrons requires information about the response functions of the dose of all the spectrometer layers to mono-energetic particle fluxes. The response matrix R_{ij} was calculated using the Monte Carlo multi-particle transport code FLUKA [43, 44] in the energy region between 100 keV and 100 MeV for electrons. The real geometry of the experimental set-up and environment were recreated for the simulations with help of the FLAIR interface for FLUKA. The approximate dose values for 20 energy intervals with different interval widths $\Delta E = [0.1; 0.175; 0.25; 0.375; 0.5; 0.75; 1; 1.75; 2.5; 3.75; 5; 7.5; 10; 15; 20; 25; 30; 40; 50; 75; 100]$ MeV were calculated by the equation $D_{i\,\mathrm{calc}} = \sum_{j=1}^{20} \Phi_j(E) R_{ij} \Delta E_j$ with an electron fluence $\Phi j(E)$ and an average response R_{ij} of a channel i over the energy interval ΔE_j. For the calculation of the electron spectrum, an unfolding-algorithm was created and applied, since the analytical calculation is impossible due to an inverse problem. The electron fluence idepending on energy was approximated by a Maxwell distribution function with two electron temperatures T_1 and T_2 and corresponding absolute numbers of electrons N_1 and N_2: $\mathrm{d}N/\mathrm{d}E_j = N_1/T_1 \times \exp(-E_j/T_1) + N_2/T_2 \times \exp(-E_j/T_2)$. The unfolding-algorithm was based on a sequential enumeration of matching data series and performed a best possible curve matching with the

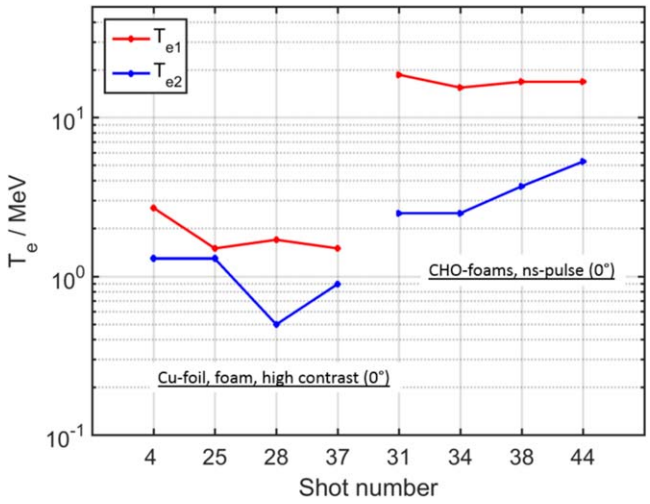

Figure 7. Electron temperatures evaluated from the measured TLD-doses via the best-fit procedure using FLUKA-simulations that accounted for a real geometry of the experimental set-up and the environment and used a two electron temperatures approximation. The best fit was achieved by keeping the deviations of the simulated doses from measured values below 10% for all 10 detector channels simultaneously.

calculation of errors for deviations between the experimental and the simulated dose values. According to the above-written equation the spectral fluence was retrieved with a precision better than 10%.

Figure 7 shows the resulting values of T_{e1} and T_{e2} for selected laser shots: N° 31, 34, 38, 44 were made onto pre-ionized foam and 4, 25, 28, 37 onto foil/foam at highest laser contrast. As expected, in the case of foams, when the TLD doses reached their maximum value, both electron temperatures are essentially higher compared to T_{e1} and T_{e2} evaluated for the case of high contrast shots. These results show a very good correlation with the experimental conditions and with the results of the electron spectrometers. The measured doses allow retrieving the absolute numbers of electrons N_1 and N_2 that interacts with the flange and produce a signal inside the TLD-cards. According to the set-up geometry, these are electrons that propagate along the x-axis with a divergence $\theta = 3.3^{\circ}$ (half angle). In the case of the laser interaction with pre-ionized foams, the best fit of all ten TLD-signals was obtained for $T_1 \backsimeq 12$ MeV and $N_1 = 0.5\text{–}1 \times 10^{10}$ electrons. This number corresponds to up to 8–16 nC of the well-directed super-ponderomotive electron beam.

4. Results of modeling and comparison with experimental data.

3D PIC simulations were performed using the virtual laser plasma Laboratory code [45] for the laser parameters and interaction geometry used in the experiment (section 1, figure 1). In particular, the FWHM axes of the elliptical laser focal spot were 13.4 and 18.8 μm, the laser pulse energy in the focal spot was 54 J (full pulse energy 94 J) and the FWHM pulse duration was of 700 fs. Resulted laser pulse intensity reached 4.4×10^{19} W cm^{-2} ($a_L = 5.67$). The plasma was composed of electrons, fully ionized ions of carbon, hydrogen and oxygen. Simulations accounted for the ion type and the ion fraction in accordance with the chemical composition of triacetate cellulose $C_{12}H_{16}O_8$, see e.g. [30]. The simulation box had a size of 610 μm along the x-axis. The first 10 and the last 100 μm of the space in this direction were free of the plasma at the initial moment. The box had 100 μm size both along the y-axis and the z-axis. Sizes of a numerical cell were 0.05 μm along the x-axis and 0.5 μm along the y-axis and the z-axis. The number of particles per cell equalled 4 for the electrons and 1 for the ions of each type. Boundary conditions were absorbing for particles and fields in each direction.

The initial electron density profile (together with the neutralizing ion density) at the moment of the main pulse arrival consisted of two parts: 2/3 of mass had a plane density distribution with initial critical electron density $n_{cr} = 10^{21}$ cm^{-3} and 1/3 had a linearly ramped profile that expands into the laser pulse direction, $n_e = (0.1 + 0.9\,(x - 10)/250)\,n_{cr}$ for $x < 260$ μm and $n_e = n_{cr}$ for x $\geqslant$ 260 μm. This electron distribution was chosen as a result of 1D hydrodynamic (HD) simulations of the 1.5 ns laser pulse interaction with 2 mg cm^{-3} homogeneous 500 μm thick layer made with a code RADIAN [35]. Results of HD-simulations made for the initially homogeneous NCD-slab were corrected to the homogenization time that is required to convert low density micro-structured matter into homogeneous NCD plasma [39, 40]. PIC-simulations were made as well for a step-like density profile with n_{cr} and 0.5 n_{cr} [30, 31]. The simulations result into a very similar behavior of the energy and angular distributions of super-ponderomotive electrons in all mentioned cases.

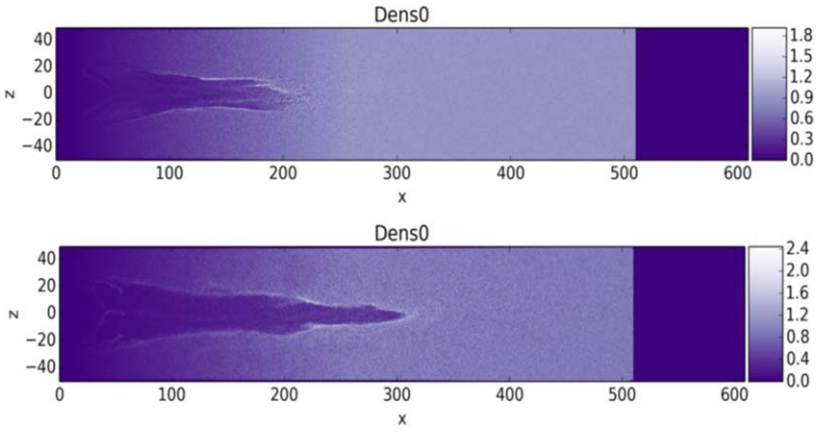

Figure 8. Snapshots of the electron density distributions in the plane XZ (see figure 1) at the time moments corresponded to $ct = 150$ and 550 μm ($t = 0$ corresponds to the laser pulse maximum at the target front side). The electron density is normalized to n_{cr}.

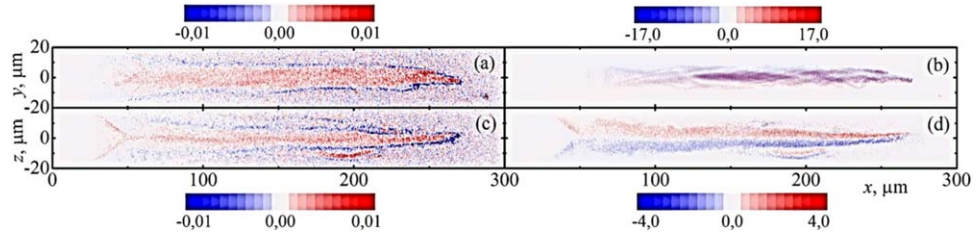

Figure 9. The electron current density j_x normalized to $n_{cr}ec$ in the plane $z = 0$ (a) and $y = 0$ (c); the components of magnetic field normalized to $(mc\omega_L)/|e|$: b_z in the plane $z = 0$ (b) and b_y in the plane $y = 0$ (d) at $ct = 250$ μm. Here m and e are the mass of electron at rest and its charge, c is the speed of light and ω_L is the laser frequency. For the laser wave length $\lambda_L = 1$ μm a dimensionless magnetic field $|b| = 1$ corresponds to 107 MG.

Figure 8 illustrates the plasma electron density dynamics during the laser pulse propagation in the plasma channel for two moments corresponding to $ct = 150$ and 550 μm (note that at $t = 0$ the laser pulse has its maximum intensity at the target front side). The creation of a plasma channel together with a strong self-focusing, filamentation and bifurcation of the laser pulse are seen in figure 8.

The presence of self-generated fields is the characteristic feature of a laser pulse channeling in plasma caused by the relativistic and ponderomotive effects. Ponderomotive expulsion of background plasma electrons from the channel creates a radial quasi-electrostatic field, while the current of the accelerated electrons generates an azimuthal magnetic field [25, 26, 30, and 31]. The structure of the electron current density along the laser propagation axis, as well as the two components of the magnetic field in the plasma channel are shown in figure 9 for $ct = 250$ μm. For the laser pulse electric field polarized along OY axis (see figure 1), the z-component of the magnetic field b_z shown in figure 9(b) contains mainly a laser field strongly increased by the self-focusing effect. At the same time, the y-component of the magnetic field b_y shown in figure 9(d) corresponds mainly to the quasistatic azimuthal magnetic field produced by a current of accelerated electrons (see figures 9(a), (c)). This field can hold fast electrons inside the channel. In particular, for 30 MeV electrons moving in a 100 MG azimuthal magnetic field, which corresponds to the dimensionless z-component $|b_z| \approx 1$ in figure 9(d), the Larmor radius is equal to 9.4 μm. This value is close to the radius of the electron current in figures 9(a), (c), which indicates the ability of the generated quasistatic magnetic field to hold the accelerated electrons in the plasma channel.

An additional focusing force for accelerated electrons can be provided by a quasistatic electric field caused by the decreased electron density in the plasma channel. Electrons trapped in the plasma channel and experiencing betatron oscillations can get in phase with the laser field and accelerated further [25, 26, and 31]. A more detailed discussion of electron acceleration mechanisms in a relativistic plasma channel based on a three-dimensional PIC simulation will be done in the next article.

The transverse electron momentum obtained in the process of acceleration determines the angular distributions of accelerated electrons shown in figure 10. A comparison of the angular distribution of accelerated electrons without restriction on the energy (depicted in figure 10(a)) with distributions at higher energies,

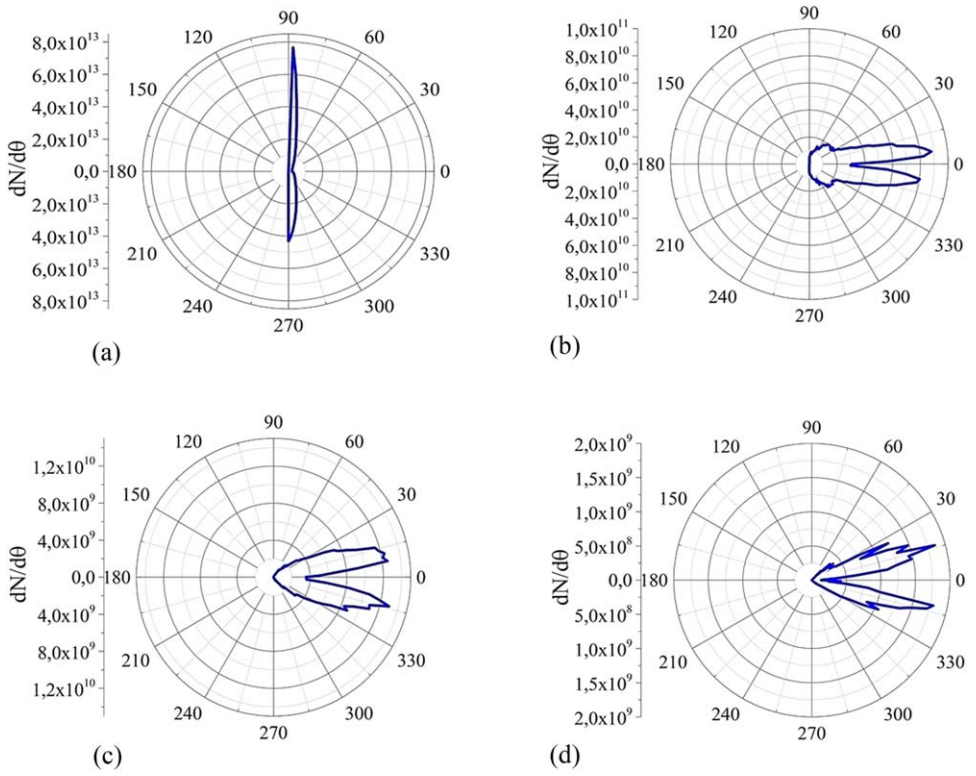

Figure 10. Distributions over angle $\theta = \mathrm{arctg}(p_z/p_x)$ of electrons, which left the target with $p_x > 0$ and $|p_y| < 0.1mc$, at the time moment corresponding to $ct = 550$ μm for different energy ranges: $(0, \infty)$ (a); (3, 12) MeV (b); (12, 100) MeV (c) and (30, 100) MeV (d).

figures 10(b)–(d), shows that the main part of relatively low energy electrons ($E < 3$ MeV) are accelerated mostly in the radial direction by a ponderomotive force that pushes electrons out of the plasma channel.

Super-ponderomotive electrons ($E > 3$ MeV) that experience the betatron oscillatons and the DLA in the plasma channel [25] leave the plasma under the angle to the direction of the laser propagation axis OX; this angle is determined by the ratio of the transversal electron momentum p_y and p_z to the longitudinal p_x. Increasing of the angle under which electrons with higher energies move relative to the laser propagation axis OX (compare figure 10(b) with (c) and (d)), reflects an increased transverse momentum of electrons accelerated by the laser pulse due to transverse betatron oscillations in the self-generated quasi-static electric and magnetic fields of the plasma channel.

We would like to emphasize that the 3D capability of the PIC code allows simulations that are close to real experimental conditions. Thus, the absolute energy spectra, i.e. the number of accelerated electrons in any energy range, and also its angular distribution can be obtained. The electron spectra were simulated at the ranges of angles $\theta = \mathrm{arctg}(p_z/p_x) = 18^\circ \pm 5^\circ$ (magenta line) and $44^\circ \pm 5^\circ$ (blue line), which correspond to the positions of the ES1 and ES2 spectrometers (figure 10). For 4.4×10^{19} W cm^{-2} ($a_L = 5.67$) vacuum laser intensity, high energy parts of the electron energy distributions ($E > 25$ MeV) simulated under 18° and 44° to the laser pulse propagation direction were approximated by the Maxwell-like functions with effective hot electron temperatures $T_h = 17.7$ MeV and 12.2 MeV. Note that in our simulations we used slightly smaller pulse duration, 700 fs, than the average value of 750 ± 250 fs indicated for the range operated in the experiment. Increasing of the pulse duration together with some decreasing of the pulse energy in the confidence intervals will lead to decrease of the laser intensity and consequently to lower hot electrons temperatures as it was checked in simulations. The square root scaling of the T_h with the laser intensity suggested in [25] would lead to $T_h = 12$ MeV ($\theta = 18^\circ \pm 5^\circ$) and 8.6 MeV($\theta = 44^\circ \pm 5^\circ$) for 2.1×10^{19} W cm^{-2} that represents the low limit of the confidential interval of laser intensities used in the experiment (see section 2). These numbers are in a good agreement with direct measurements of the electron energy distributions resulting in $T_h = 12.8$–13 MeV ($\theta = 18^\circ \pm 5^\circ$) and 7.5–8.0 MeV ($\theta = 44^\circ \pm 5^\circ$), see figure 5(a).

The 3D geometry of the simulations that was chosen in conformity with the experimental set-up allows obtaining not only the shape of the spectra and realistic angular distributions, but also the absolute numbers of accelerated particles. Taking into account the solid angle, under which the electron spectrometer ES1 is seen, the

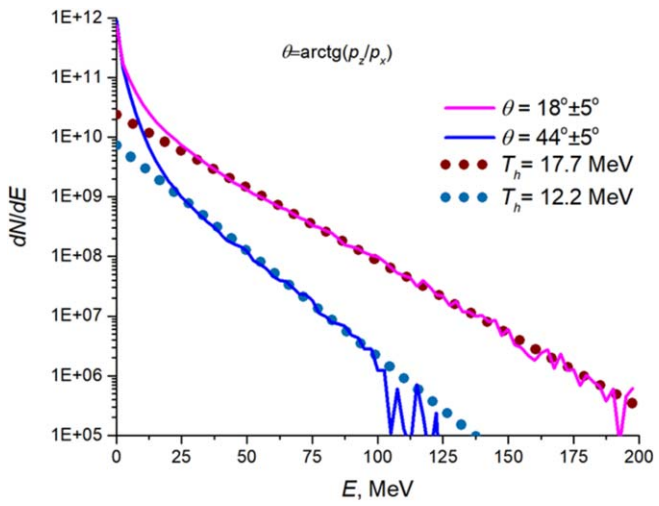

Figure 11. Electron energy spectra obtained in PIC simulations at 4.4×10^{19} W cm^{-2} ($a_L = 5.67$) for spectrometers ES1 and ES2 at the ranges of angles $\theta = \mathrm{arctg}(p_z/p_x) = 18^\circ \pm 5^\circ$ (magenta line) and $44^\circ \pm 5^\circ$ (blue line). Brown and green dotted lines are exponential fits for effective temperatures $T_h = 17.7$ and 12.2 MeV.

Table 1. Energy dependent number, charge and conversion efficiency of accelerated electrons which left the target with $p_x > 0$ at $ct = 550$ μm predicted by PIC-simulations.

Energy range, MeV	Number of electrons	Charge of electrons, μC	Percent of laser energy
$(0.5, +\infty)$	3.22×10^{13}	5.15	40%
$(3, +\infty)$	1.15×10^{13}	1.84	31%
(3, 12)	9.09×10^{12}	1.45	14.8%
$(12, +\infty)$	2.38×10^{12}	0.381	16.3%
$(30, +\infty)$	4.85×10^{11}	0.078	6.4%

number of electrons reaching the spectrometer with energies above 30 MeV is 6×10^5, as follows from figure 10(d).

Similar number of electrons can be estimated from figure 11 for the range of angles $\theta = \mathrm{arctg}(p_z/p_x) = 18^\circ \pm 5^\circ$ (magenta line), taking into account that the energy spectrum accumulates particles with any transverse momenta p_y. The obtained number of electrons with energies above 30 MeV 6×10^5, coincides rather well with the number measured by the electron spectrometer ES1 in shot 44 (3×10^5, see figure 5(b)). Table 1 presents the total number of electrons, their charge and corresponding conversion efficiency for different intervals of electron energies obtained in PIC-simulations. The total charge of electrons with energies above 3 MeV reaches 2 μC, while the charge of super-ponderomotive electrons with $E > 30$ MeV reaches a very high value of 78 nC.

In recent simulations [46], 30 fs, 4 J laser pulse of 8×10^{20} W cm^{-2} intensity interacted with an ionized planar target. A target electron density was varied from 0.05 n_{cr} up to 2 n_{cr} and a layer thickness from 10λ up to 500λ. The authors reported an ability to generate up to 7 nC total charge of electrons accelerated to energies above 30 MeV. This number corresponds to 1.7 nC per 1 J of the input laser energy. The achieved efficiency is very close to our result (78 nC at 54 J in the focal spot, see table 1) obtained at much lower laser intensity of 4.4×10^{19} W cm^{-2} for 700 fs laser pulse duration. A high available energy of sub-picosecond laser pulses (~100 J) makes it possible to generate a high total charge of accelerated electrons. The number of accelerated electrons with energies above 30 MeV can reach a 300 nC level. This result was obtained in [31] for the case of a $(0.5 \div 2)$ n_{cr} plasma layer and a 700 fs, 120 J laser pulse with an intensity of 5.7×10^{20} W cm^{-2}, focused into a 4 μm focal spot, and corresponds to an efficiency of 2.5 nC per 1 J of the full input laser energy.

5. Conclusion

In this article, we present new experimental results on the interaction of relativistic sub-picosecond laser pulses with extended, sub-mm long NCD-plasmas. Low density polymer foam layers were used to create this type of hydrodynamic stable, large scale, quasi-homogeneous plasmas. Interaction of the relativistic laser pulse with large-scale NCD-plasmas ensures a long acceleration path and results into effective coupling of the laser energy into energetic electrons.

Experiments on the electron heating by a 80–100 J, 750 fs short laser pulse of 2–5 $\times$ 10^{19} W cm^{-2} intensity demonstrated that the effective temperature of supra-thermal electrons increased from 1.5–2 MeV, in the case of the relativistic laser interaction with a metallic foil at high laser contrast, up to 13 MeV for the laser shots onto the pre-ionized 300–500 μm long foam layer with a NCD. The measurements showed high directionality of the acceleration process.

The observed tendency towards the strong increase of the mean electron energy and number of super-ponderomotive electrons is reinforced by the results of the gamma-yield measurements. In the case of laser interaction with long-scale NCD-plasmas, the dose caused by the gamma-radiation measured in the direction of the laser pulse propagation showed a 1000-fold increase compared to the high contrast shots onto plane foils and doses measured perpendicular to the laser propagation direction for all used combinations of targets and laser parameters. The effective temperature of super-ponderomotive electrons retrieved from the measured TLD-doses by means of the Monte-Carlo simulations reached 11–12 MeV, which is in a good agreement with direct measurements by the electron spectrometers.

The experiment was supported by the full 3D-PIC simulations that account for the used laser parameters and the geometry of the experimental set-up and allow, in contrast to usually used 2D-3V PIC analysis, simulating the absolute number of accelerated electrons, their energy and angular distributions. The obtained simulation results are in a good agreement with measured amount of electrons that were registered by the electron spectrometers and indicate the effective electron acceleration in NCD plasmas with a total electron charge of about 2 μC at the energies above ponderomotive one (>3 MeV), while the charge of super-ponderomotive electrons with $E > 30$ MeV reaches a high value of 80 nC.

Acknowledgments

The theoretical part of the work was supported by the Presidium of the Russian Academy of Sciences (Programme 'Extreme Light Fields and Their Interaction with Matter'). The experimental group is very thankful for the support provided by the PHELIX-laser team at GSI-Darmstadt and by RFBR 17-02-00366 project. We would like to thank Dr Galina Vergunova, Lebedev Physical Institute, Moscow for hydrodynamic simulations of the direct foam heating by ns laser pulse.

References

[1] Le P S *et al* 2010 *Phys. Plasmas* **17** 056309
[2] Morace A *et al* 2014 *Phys. Plasmas* **21** 102712
[3] Tahir N A *et al* 2005 *Phys. Rev. Lett.* **95** 035001
[4] Tahir N A *et al* 2010 *New J. Phys.* **12** 073022
[5] Ravasio A *et al* 2008 *Phys. Plasmas* **15** 060701
[6] Li K *et al* 2014 *Laser Part. Beams* **32** 631
[7] Brunel F 1987 *Phys. Rev. Lett.* **59** 52
[8] Wilks S C, Kruer W L, Tabak M and Langdon A B 1992 *Phys. Rev. Lett.* **69** 1383
[9] Gibbon P 2005 *Short Pulse Laser Interactions with Matter: An Introduction* (London/Singapore: Imperial College Press/World Scientific)
[10] Mulser P and Bauer D 2010 *High-Power Laser-Matter Interaction* (Heidelberg: Springer)
[11] Mulser P, Weng S M and Liseykina T 2012 *Phys. Plasmas* **19** 043301
[12] Bochkarev S G *et al* 2014 *Plasma Phys. Rep.* **40** 202–14
[13] Andreev N E, Pugachev L P, Povarnitsyn M E and Levashov P R 2016 *Laser Part. Beams* **34** 115–22
[14] Andreev N E *et al* 2011 *Plasma Phys. Control. Fusion* **53** 014001
[15] Leemans W P *et al* 2014 *Phys. Rev. Lett.* **113** 245002
[16] Esarey E, Schroeder C B and Leemans W P 2009 *Rev. Mod. Phys.* **81** 1229
[17] Faure J *et al* 2004 *Nature* **431** 541–4
[18] Pugacheva D V and Andreev N E 2018 *Quantum Electron.* **48** 291
[19] Walker P A *et al* 2013 *New J. Phys.* **15** 045024
[20] Ju J *et al* 2014 *Phys. Rev. ST Accel. Beams* **17** 051302
[21] Willingale L *et al* 2011 *Phys. Plasmas* **18** 056706
[22] Willingale L *et al* 2013 *New J. Phys.* **15** 025023
[23] Toncian T *et al* 2016 *Matter Radiat. Extremes* **1** 82–7
[24] Willingale L *et al* 2018 *New J. Phys.* **20** 093024

[25] Pukhov A, Sheng Z-M and Meyer-ter-Vehn J 1999 *Phys. Plasmas* **6** 2847
[26] Borghesi M *et al* 1998 *Phys. Rev. Lett.* **80** 5137
[27] Arefiev A V *et al* 2016 *Phys. Plasmas* **23** 056704
[28] Khudik V *et al* 2016 *Phys. Plasmas* **23** 103108
[29] Gray R J *et al* 2014 *New J. Phys.* **16** 113075
[30] Pugachev L P, Andreev N E, Levashov P R and Rosmej O N 2016 *Nucl. Instrum. Methods Phys. Res.* A **829** 88
[31] Pugachev L P and Andreev N E 2018 *J. Phys.: Conf. Ser.* **1147** 012080
[32] Khalenkov A M *et al* 2006 *Laser Part. Beams* **24** 283
[33] Borisenko N G *et al* 2006 *Fusion Sci. Technol.* **49** 676
[34] Borisenko N G *et al* 2007 *Fusion Sci. Technol.* **51** 655
[35] Vergunova G A *et al* 2013 *Plasma Phys. Rep.* **9** 755–62
[36] Faik S *et al* 2013 *High Energy Density Phys.* **10** 47–55
[37] Rosmej O N *et al* 2015 *Plasma Physics Control. Fusion* **57** 094001
[38] Horst F *et al* 2015 *Nucl. Instrum. Methods Phys. Res.* A **782** 69
[39] Gus'kov Y, Limpouch J, Nicolai P and Tikhonchuk V T 2011 *Phys. Plasmas* **18** 103114
[40] Nicolaï Ph *et al* 2012 *Phys. Plasmas* **19** 113105
[41] Bonnet T *et al* 2013 *Rev. Sci. Instrum.* **84** 103510
[42] Tanaka K A *et al* 2005 *Rev. Sci. Instrum.* **76** 013507
[43] Böhlen T T *et al* 2014 *Nucl. Data Sheets* **120** 211–4
[44] Ballarini F, Battistoni G, Campanella M *et al* 2006 *J. Phys.: Conf. Ser.* **41** 151
[45] Pukhov A 1999 *J. Plasma Phys.* **61** 425–33
[46] Lobok M G, Brantov A V, Gozhev D A and Bychenkov V Y 2018 *Plasma Phys. Control. Fusion* **60** 084010